2019

Analysis of surface roughness evolution of ferritic stainless steel using crystal plasticity finite element method

Xiaoguang Ma
University of Wollongong, xm966@uowmail.edu.au

Jingwei Zhao
University of Wollongong, jzhao@uow.edu.au

Wei Du
Baoshan Iron and Steel

Xin Zhang
Baoshan Iron and Steel, xzhang@uow.edu.au

Zhengyi Jiang
University of Wollongong, jiang@uow.edu.au

Analysis of surface roughness evolution of ferritic stainless steel using crystal plasticity finite element method

Abstract

In order to evaluate the surface quality of ferritic stainless steel (FSS) sheets tensile deformation, a crystal plasticity (CP) model, in which the constitutive laws were incorporated with the consideration of the heterogeneous distribution of the properties of grains, was established to analyse the effect of texture, grain sizes and initial surface roughness on the surface roughness evolution of FSS sheets. The electron backscatter diffraction (EBSD) tests were performed to characterise the texture and the grains. A tensile test of the represent volume was simulated and further verified by experimental results. The numerical simulation results indicate that the surface roughness is dependent almost linearly on the average grain size. The {001}(110) and the {112}(110) components induce remarkable undulation on the surface of FSS sheets during uniaxial tension. The surface topology of FSS sheets after tensile deformation are obtained using 3D laser scanning microscope, which shows an agreement with the simulated results.

Disciplines

Engineering | Science and Technology Studies

Publication Details

Ma, X., Zhao, J., Du, W., Zhang, X. & Jiang, Z. (2019). Analysis of surface roughness evolution of ferritic stainless steel using crystal plasticity finite element method. Journal of Materials Research and Technology, 8 (3), 3175-3187.

Available online at www.sciencedirect.com

jmr&t Journal of Materials Research and Technology

www.jmrt.com.br

Original Article

Analysis of surface roughness evolution of ferritic stainless steel using crystal plasticity finite element method

Xiaoguang Ma[a,*], Jingwei Zhao[a,*], Wei Du[b], Xin Zhang[b], Zhengyi Jiang[a,*]

[a] School of Mechanical, Materials, Mechatronic and Biomedical Engineering, University of Wollongong, Wollongong, NSW 2522, Australia
[b] Stainless Steel Technical Centre, Baosteel Research Institute (R&D Centre), Baoshan Iron & Steel Co., Ltd., Shanghai 200431, China

ARTICLE INFO

Article history:
Received 21 September 2018
Accepted 27 March 2019
Available online 21 May 2019

Keywords:
Ferritic stainless steel
Surface roughness evolution
Surface topography
Crystal plasticity model.

ABSTRACT

In order to evaluate the surface quality of ferritic stainless steel (FSS) sheets tensile deformation, a crystal plasticity (CP) model, in which the constitutive laws were incorporated with the consideration of the heterogeneous distribution of the properties of grains, was established to analyse the effect of texture, grain sizes and initial surface roughness on the surface roughness evolution of FSS sheets. The electron backscatter diffraction (EBSD) tests were performed to characterise the texture and the grains. A tensile test of the represent volume was simulated and further verified by experimental results. The numerical simulation results indicate that the surface roughness is dependent almost linearly on the average grain size. The {001}⟨110⟩ and the {112}⟨110⟩ components induce remarkable undulation on the surface of FSS sheets during uniaxial tension. The surface topology of FSS sheets after tensile deformation are obtained using 3D laser scanning microscope, which shows an agreement with the simulated results.

1. Introduction

For ferritic stainless steels (FSSs), surface roughening is an undesirable phenomenon in manufacturing engineering. During the forming process, the FSS sheets show profound undulations at different positions without fluctuations in the thickness direction. The increased surface roughness deteriorates the appearance of the formed product, and even affects the surface properties such as the reflectivity, lubricant transport, weldability, adhesion and mechanical properties due to the strain localisation [1]. In order to reduce the surface roughness and improve the surface quality of the formed products, the surface roughening phenomenon has been extensively studied by researchers using both numerical simulation and experimental methods. Takechi et al. [2] proposed a numerical model with crystal plasticity (CP) theories, and the effects of different shear strains between RD//⟨110⟩ fibres were investigated based on both numerical and experimental results. Wright [3] studied the plastic–strain ratios between the {111}⟨112⟩ matrix and the {001}⟨110⟩ band. It was found that the different plastic strain ratios between the {111}⟨112⟩ and the {001}⟨110⟩ components contributed to the

* *Corresponding authors.*
E-mails: xm966@uowmail.edu.au (X. Ma), jwzhaocn@gmail.com (J. Zhao), jiang@uow.edu.au (Z. Jiang).
https://doi.org/10.1016/j.jmrt.2019.03.017

surface roughening during the forming process. Shin et al. [4] investigated the surface roughening evolution of FSS when subjected to tensile deformation and found that the lower plastic strain ratio of the {001}⟨110⟩ components and different shear deformations of the {111}⟨110⟩ or {112}⟨110⟩ components contributed to the development of surface roughening of FSS sheets. A new finite element method (FEM) was proposed by Knutsen and Wittridge [5] in order to account for the occurrence of parallel corrugations on the surface of FSS during uniaxial tensile straining. The results indicate that parallel surface corrugation profile was mainly dependent on the local anisotropy in plastic behaviour. Jung et al. [6] evaluated the effect of coarse precipitates on surface roughening of aluminium alloys using crystal plasticity finite element method (CPFEM). The numerical simulation results show that the precipitates act differently depending on the spatial distribution of kinematically weak and strong orientations. Shi et al. [7] quantitatively associated surface roughening with single CP theories and spatial grain orientation distribution, and found that the banding of the Cube and the Goss components are responsible for the profound surface roughening of aluminium alloy AA 6xxx. A new surface roughening model was developed by Engler [8] to study the effect of recrystallisation texture orientations on surface roughening evolution. The band-like clusters of grains with similar crystal orientations was found to promote undulations on the surface. In addition, Huh et al. [9] proposed a CPFEM in order to quantitatively describe the surface roughing of FSS 430 after tensile test. Both simulated and experimental results indicated that the out of plane shear and spatial variations in through-thickness strains were the most common causes of the observed ridging behaviour. With different plastic–strain ratios and Taylor factors, the neighbouring grains in polycrystalline materials tend to show different plastic deformations after tension or deep-drawn, leading to remarkable surface corrugations and surface roughening.

Except for texture, it is commonly acknowledged that the grain size also affects the surface roughness after plastic deformation [10–13]. Stoudt and Ricker [10] investigated the relationship between the grain size and the surface roughening behaviour of Al–Mg alloys, and stated that the roughening rate was dependent on the grain size. In addition, Stoudt et al. [11] studied the correlation between deformation-induced surface roughness and plastic strain in AA 5754. It was found that the fine grain size produced a linear relationship between the surface roughness and plastic strain. The evolution of surface roughness during deformation of polycrystalline aluminium alloys was systematically studied by Wouters et al. [12] using a height–height correlation technique. The results indicated that the observed roughness was induced by a combination of self-affine roughening on a subgrain scale and a grain scale roughening caused by orientation differences between neighbouring grains. A linear relationship between the root-mean square surface roughness and grain size was also found in experiments. The effect of average grain size on surface roughness evolution during tension test was analysed by Ma et al. [13] using both numerical simulation and experimental methods. The coarser grain size was found to induce remarkable undulations on the surface of FSS after tension performance. As the grain size increased, the irregularity generated from rotation and slip of grains can be dominant, inducing the surface defections on the formed products.

In order to improve the surface quality of the formed products, understanding of the surface roughness evolution is considered to be critical in developing strategies to enhance the resistance against the surface roughening. Lefebvre et al. [14] evaluated the effect of the spatial distribution of crystallographic orientations on roping amplitude and wavelength in FSS using the viscoplastic fast Fourier transform model. Saleh et al. [15] analysed the microstructure and texture evolution in a twinning-induced-plasticity steel during uniaxial tension with proposed visco-plastic self-consistent model, and found that the effect of the perfect slip was dominant compared with twinning on the texture formation. A moving window approach was proposed by Qin et al. [16] to understand the macroscopic surface roughening based on the spatial distribution of grains belonging to specific individual orientations. It was stated that the difference in the *r*-value between neighbouring grains contributed to the surface roughening. A step-by-step method was proposed by Romanova et al. [17] to evaluate the surface hardening effect on the deformation-induced roughening in polycrystals. The authors stated that the presence of the surface-hardened layer in polyscrystalline structure caused a delay in the development of surface roughness and reduced its growth rate.

Although a number of models were built to investigate the surface roughening evolution of polycrystalline materials after tensile deformation, the effect of initial surface roughness and orientation distribution are not yet comprehensively investigated. In this study, both the measured initial surface profile and the key texture components are incorporated into the FE modelling to enhance the accuracy of simulated results. In order to further investigate the relationship between the surface roughening and grain properties of FSS sheets, a crystal plasticity finite element model is established and adopted to simulate the evolution of the surface roughness of FSS 430 during uniaxial tensile tests. All the simulated results are verified by the uniaxial tensile tests.

2. FE simulation models

2.1. *Crystal plasticity theory*

The localised deformation in ductile single crystals was analysed by Pierce et al. [18]. It is commonly acknowledged that the plastic deformation of polycrystalline materials is affected by a combination of crystallographic dislocation slip, twinning, diffusion and grain boundary sliding. In comparison to slip, however, the effect of twinning, diffusion and grain boundary sliding on plastic strain can be negligible. For this reason, the total deformation gradient can be described by the combination of elastic and plastic components:

$$F = F^e \cdot F^p \tag{1}$$

where F^e represents the plastic shear of the material, and F^p means the stretching and rotation of the lattice. It is assumed that the elastic properties cannot be affected by slip, the stress,

therefore, is determined by F^p. The velocity gradient in this state is:

$$L^p = F^p F^{p-1} = \sum \gamma^\alpha S_0^\alpha \tag{2}$$

$$S_0^\alpha = m^\alpha \otimes s^\alpha \tag{3}$$

where γ^α is the slipping rate of the α slip system, and S_0^α is the Schmid tensor. In all activated slip systems, m^α and s^α are the slip direction and the normal to slip plane on the αth slip system, respectively. The slip direction and the normal to the slip plane of the slip system α are defined as:

$$m^{*\alpha} = F^e m^\alpha \tag{4}$$

$$s^{*\alpha} = \left((F^e)^{-1}\right)^T s^\alpha \tag{5}$$

For rate-sensitive slip systems, the slip rates can be described as functions of plastic shearing rate and resolved shear stresses based on Schmid laws [19]. The shearing rate is displayed as:

$$\gamma^\alpha = \gamma_0^\alpha \frac{\tau_0^\alpha}{g^\alpha} \left| \frac{\tau_0^\alpha}{g^\alpha} \right|^{(1/m)-1} \tag{6}$$

where γ_0^α, g^α and τ_0^α refer to the reference shear rate, slip resistance and resolved shear stress on α slip system, respectively. It is assumed that the current strain hardened state of crystal is only dependent on sip strain. The self and latent hardening function g^α is characterised by the strengths as follows:

$$g^\alpha = \sum\nolimits_\beta h^{\alpha\beta} \left|\gamma^\beta\right| \tag{7}$$

$$h^{\alpha\beta} = q^{\alpha\beta} h^\beta \tag{8}$$

where $h^{\alpha\beta}$ are the slip hardening moduli of active slip systems.

$$h^{\alpha\beta} = \left[q + (1-q)\,\delta^{\alpha\beta}\right] h^\beta \tag{9}$$

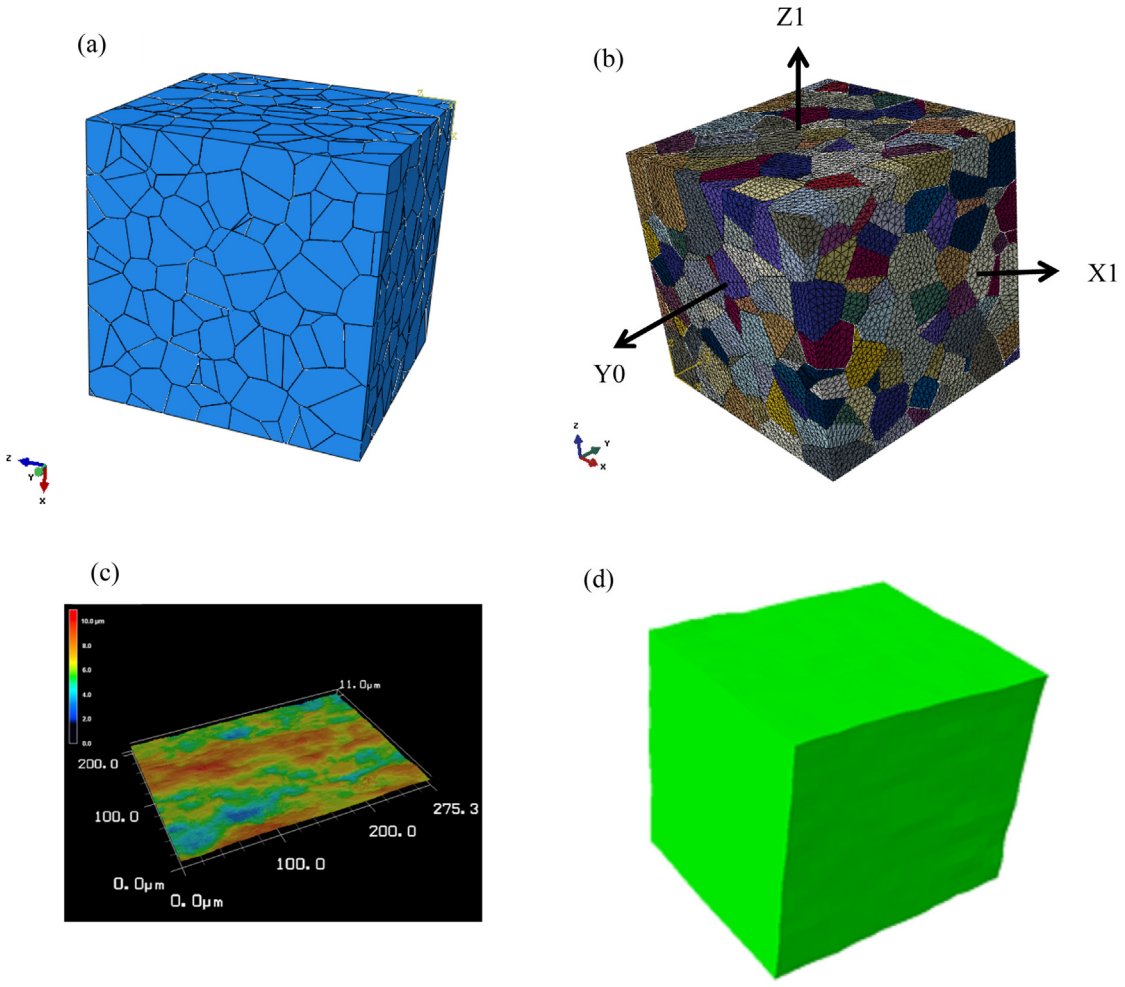

Fig. 1 – Voronoi structures and grain models: (a) Voronoi models generated with MATLAB, (b) mesh of grain model with ideal flat surface, (c) the initial surface topography observed using microscope, and (d) the model with the consideration of initial surface topography.

where q denotes the latent hardening parameter, and h^{β} denotes the hardening rate. The h^{β} can be calculated with the following equation:

$$h^{\beta} = h_0 \left(1 - \frac{g^{\beta}}{\tau_s}\right)^{\alpha} \tag{10}$$

where h_0, τ_s and α are the slip system hardening parameters used in this study. h_0 denotes the initial hardening modulus, τ_s denotes the saturation stress where large plastic flow initiates and α represents the reference strain rate. All the equations have been implemented into a user subroutine UMAT, and the programme is imported into the FE software ABAQUS for further calculation.

2.2. *Voronoi models*

In order to establish grain models with desired shapes and sizes, voronoi tessellation is utilised to describe the properties of polycrystalline aggregates. Being given a set of points $E = \{G_i(x_i)\}$ into a region of a 3D space $D \in R^3$, an arbitrary point P within the area R(i) is closer to point i than any other point, and each point G_i forms a Voronoi polyhedron based on the above mentioned laws [13]. The point G_i is associated with polyhedron C_i as:

$$C_i = \left\{P(X) \in D | d(P, G_i) < d(P,) G_j \forall j \neq i\right\} \tag{11}$$

where C_i is the Voronoi polyhedron, the norm corresponds with Euclidean distance. In grain modelling, the generated polyhedrons correspond to the recrystallised, equixed grains. Each Voronoi cell was assigned with a specific crystal orientation and unique response to deformation. Consequently, the surface roughening of established model can be affected by all grains.

Four surface roughness parameters, including the arithmetic average roughness (R_a), the root mean square roughness (R_q), the skewness (R_{sk}) and the kurtosis roughness (R_{ku}), are utilised in the present study to characterise the 3D roughness topography on the surface of FSS. The above roughness parameters can be expressed by:

$$R_a = \frac{\sum S_i \left| Z_i - \frac{\sum s_i Z_i}{\sum s_i} \right|}{\sum S_i} \tag{12}$$

$$R_q = \sqrt{\frac{\sum S_i \left(Z_i - \frac{\sum s_i Z_i}{\sum s_i} \right)^2}{\sum S_i}} \tag{13}$$

$$R_{sk} = \frac{1}{R_q^3} \left[\frac{\sum S_i \left(Z_i - \frac{\sum s_i Z_i}{\sum s_i} \right)^3}{\sum S_i} \right] \tag{14}$$

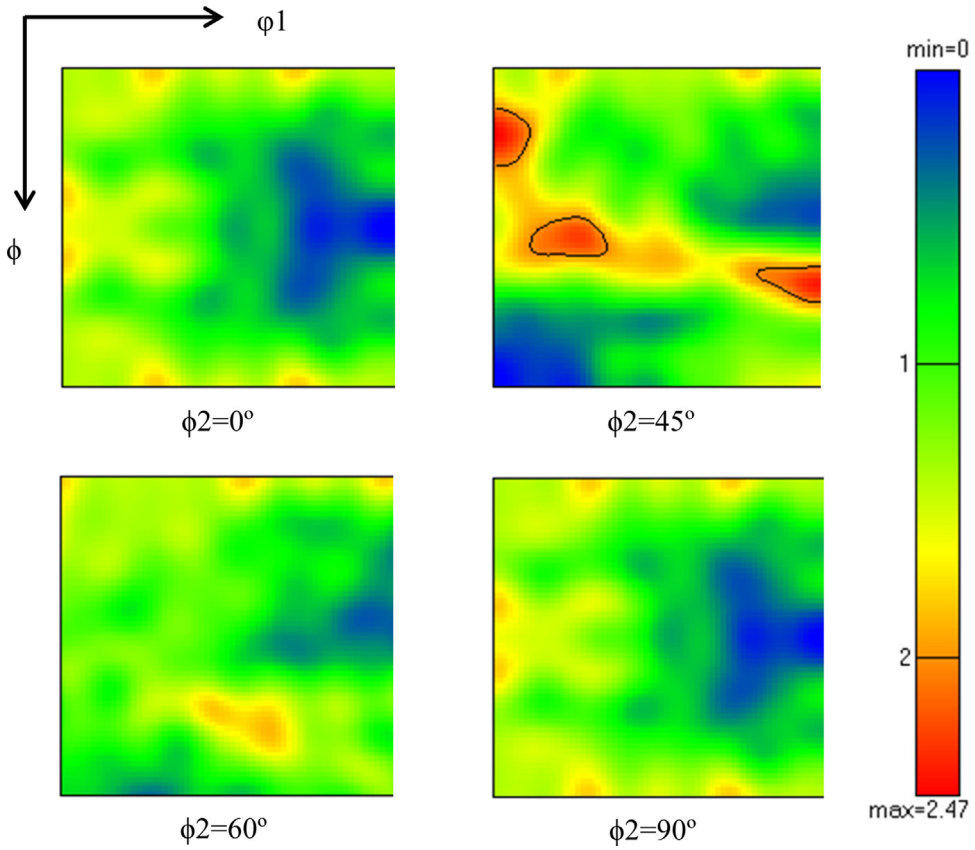

Fig. 2 – ODFs of FSS 430.

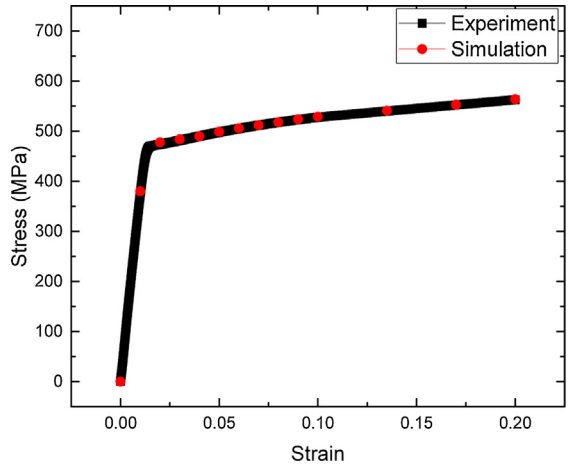

Fig. 3 – The strain–stress curves of tensile tests and numerical simulation.

$$R_{ku} = \frac{1}{R_q^4}\left[\frac{\sum S_i\left(Z_i - \frac{\sum s_i Z_i}{\sum s_i}\right)^4}{\sum S_i}\right] \quad (15)$$

where Z_i is the average asperity of height of a Voronoi cell, $\sum S_i$ is the sample area, and S_i is individual Voronoi cell. In this study, the surface topology was measured using the Keyence VK-X100-3D Laser Scanning Microscope. Three tests were repeated for each group of experiments and the mean value was calculated and utilised to evaluate the surface roughness.

The established Voronoi structures and grain models are shown in Fig. 1. Both average grain size and crystal orientation distribution function (ODF) were considered when building the FE mesh. A representative volume of a solid rectangular was formed to evaluate the surface topography of FSS. The model contained 100–1000 Voronoi polyhedrons with an arbitrary shape generated by commercial software MATLAB. The grains were meshed with four-node tetrahedral elements with linear interpolation and full integration (C3D4 elements).

In order to enhance the accuracy of the numerical simulation, crystallographic orientation distribution is considered in this model. It is commonly acknowledged that the corrugation on the surface is induced by the different plastic deformations of neighbouring grains with different crystal orientations [20–23]. The major texture components, including the {001}⟨110⟩, Cube, Goss and {112}⟨110⟩ components, have been assigned to the grains in established model. In ABAQUS user subroutine, the crystal orientation is calculated based on the matrix below:

$$g = \begin{pmatrix} \cos\phi\cos\theta - \sin\phi\sin\theta\cos\psi & \sin\phi\cos\theta + \cos\phi\sin\theta\cos\psi & \sin\theta\sin\psi \\ -\cos\phi\ \sin\theta - \sin\phi\cos\theta\cos\psi & -\sin\phi\sin\theta + \cos\phi\cos\theta\cos\psi & \cos\theta\sin\psi \\ \sin\phi\ \sin\psi & -\cos\phi\ \sin\psi & \cos\psi \end{pmatrix} \quad (16)$$

Table 1 – Key parameters used for numerical simulation.

Material properties	Values used in simulation
Young's modulus	$E = 1.94 \times 10^5$ MPa
Poisson ratio	$\mu = 0.29$
Strain rate sensitivity	$m = 0.02$
Initial value of slip resistance parameter	$g_0 = 110$ MPa
Reference strain rate	$\alpha = 0.0001$
Initial hardening modulus	$h_0 = 1700$ MPa
Stage I stress	$g = 252$ MPa
Latent hardening parameter	$q = 1.4$

Table 2 – Roughness parameters in different cases.

Case	R_a (μm)	R_q (μm)	R_{sk} (μm)	R_{ku} (μm)
1	0	0	0	0
2	0.51	0.70	1.53	10.57
3	0.82	1.07	−0.38	3.86
4	0.97	1.25	−0.04	3.70

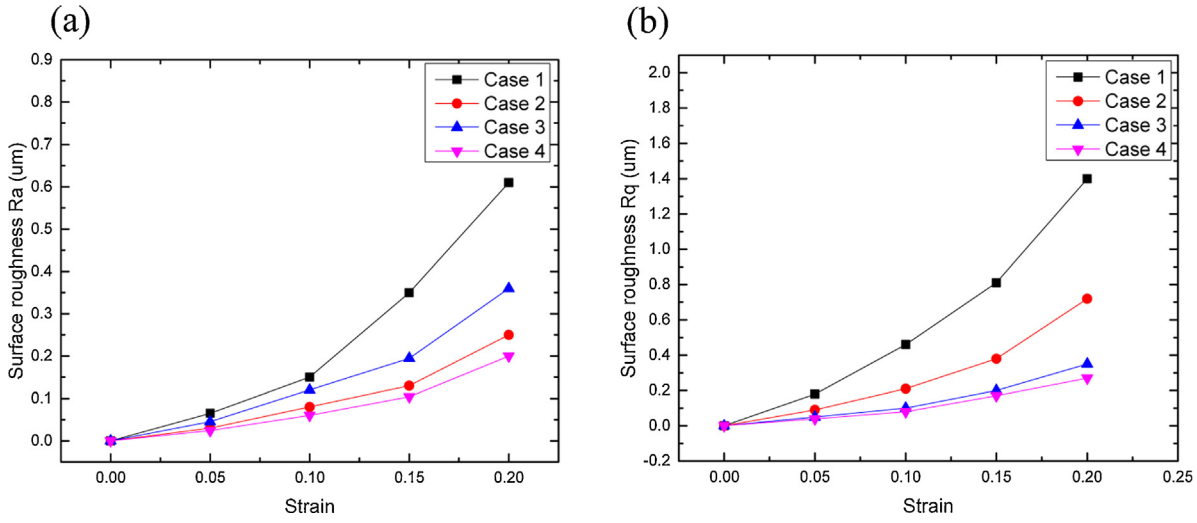

Fig. 4 – The relationship between the surface roughness and strain along RD: (a) R_a and (b) R_q.

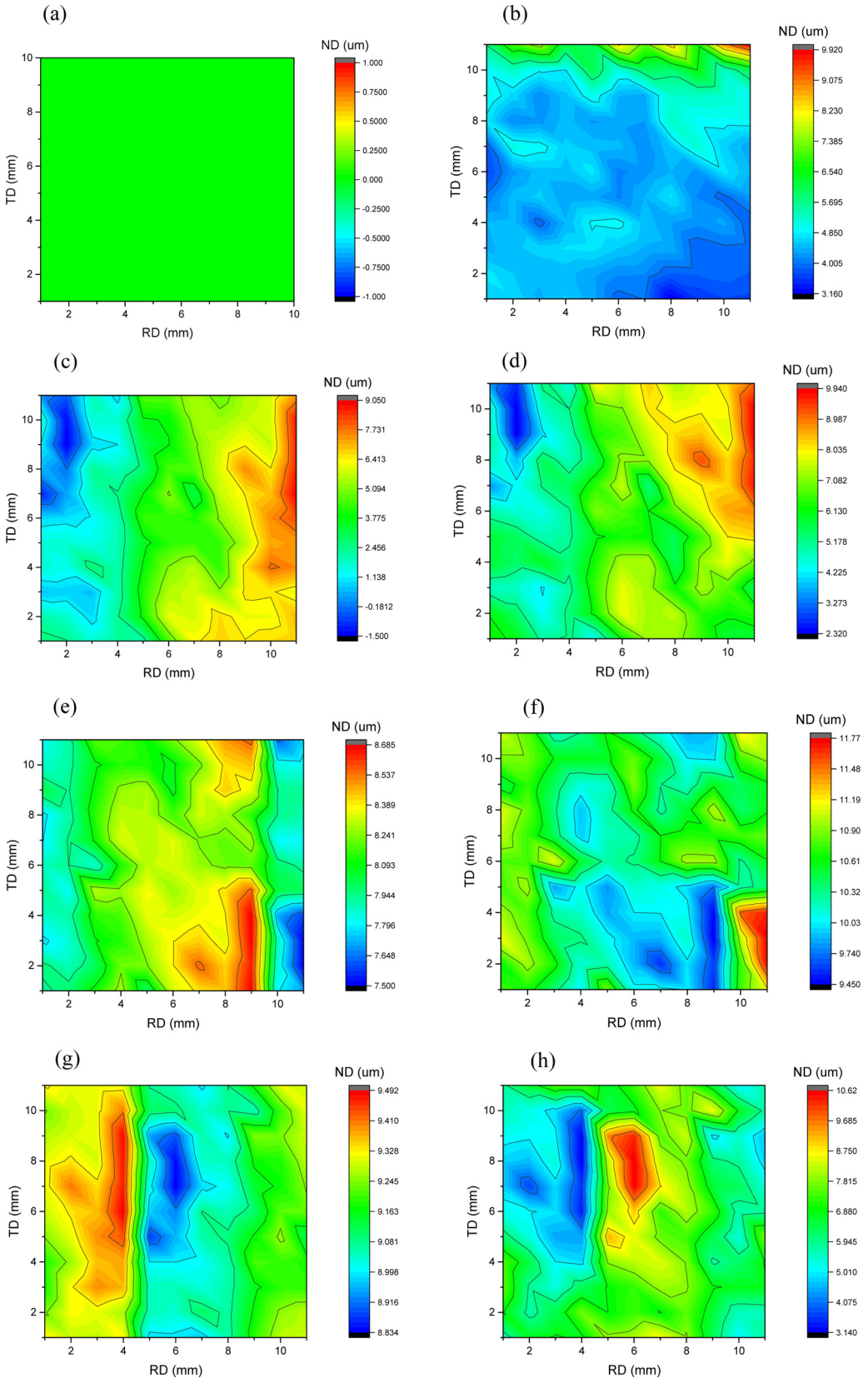

Fig. 5 – Surface topographies of the established model with different initial surface roughness: (a, c, e, g) the initial surface topography in cases 1–4 and (b, d, f, h) the final surface topography in cases 1–4.

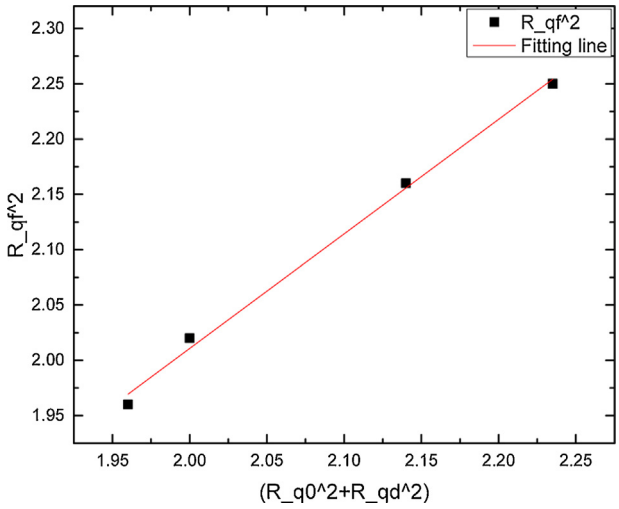

Fig. 6 – The relationship between R_{qf}^2 and $(R_{q0}^2 + R_{qd}^2)$.

where φ, θ and ψ are the Euler angles in each grain. To describe the microstructure in proposed model, the fractions of major texture components of FSS 430 is obtained from EBSD tests. Fig. 2 shows the ODFs of FSS 430. In the established model, the crystal orientations are assigned to all grains based on the fractions of major texture components obtained from EBSD tests.

2.3. *Boundary conditions*

In order to assess the surface roughness evolution during plastic deformation, a series of tensile tests were simulated along RD. As shown in Fig. 1(b), axes X, Y and Z represent RD, TD and ND of the FSS specimen, respectively. The surfaces X1, Y0 and Z1 are displayed in Fig. 1(b) and the opposite surfaces are defined to be X0, Y1 and Z0. The model is stretched along RD and the top surface Z1 is used for surface topography observation. The periodic boundary conditions are applied on surfaces X0, X1, Y0 and Y1. Five different average grain sizes are utilised in this model so that the effect of the average grain size can be analysed. Finally, two steps are applied in this model to ensure the accuracy of results. In step 1, a nominal strain $\varepsilon = 0.003$ is assigned. In step 2, a specific displacement is set along the RD. 50 increments per simulation step were used in this model to achieve the convergence and provide numerical stability.

FSS 430 is utilised in the present study. 24 slip systems are assumed to be activated during the formation process. Each grain was assigned with a specific orientation and the whole model was meshed with C3D4 (3-D, four-node, Tet) elements. The program run on computer with three microprocessors in parallel, over 10 000 steps were required to reach the convergence. Fig. 3 shows the stress-strain curves obtained from numerical simulation and experiments. The results match well with each other, indicating that the established model can be utilised to predict the surface roughness evolution of FSS 430. The key parameters in proposed model are summarised in Table 1.

3. Results and discussion

3.1. *Effects of initial surface roughness*

During the plastic deformation of polycrystalline materials, the initial surface roughness is considered to be critical in determining the surface topography. To evaluate the effect of the initial surface roughness on surface roughness evolution during deformation, a series of models with different initial surface roughness are simulated. The roughness parameters in different cases are listed in Table 2. The other key parameters remain the same in this group: (i) the average grain size of grains is 10 μm, and (ii) the model is stretched along RD with 20% extension.

Fig. 4 shows the relationship between the surface roughness and strain along RD. The variation of surface roughness ΔR_a and ΔR_q are defined as the surface roughness value after plastic deformation minus the initial surface roughness. As can be seen in Fig. 4(a) and (b), a quadratic correlation between ΔR_a (ΔR_q) and tension strain is found to describe the surface roughness evolution of FSS 430 after tension performance. For specimens with significant initial surface roughness, the variations of surface roughness are smaller. It is known that the surface roughness evolution can be attributed to the flattening and the movement of grains during uniaxial tension. For specimens with large initial surface roughness, the effect of flattening on surface roughness evolution can be dominant, causing limited increase of surface roughness during tension performance [24]. On the other hand, the surface roughness evolution of specimens with flat initial surface is significantly affected by the deformation of individual grains, therefore leads to the remarkable increase of the surface roughness after extension [13].

Fig. 5 shows the surface topographies of the established model with different initial surface roughness (cases 1–4). It can be seen from Fig. 5(a) and (b) that even for specimens with ideal flat plane, the final surface topography can be inhomogeneous after tension performance due to the movement of lattice. With different plastic strain ratio and plastic deformation of neighbouring grains, the misorientation between neighbouring grains is considered to be responsible for the surface roughness development of FSS during uniaxial tension [25–27]. Therefore, the evolution of surface roughness during tensile deformation can be represented by the homogeneous flattening and the inhomogeneous lattice movement.

To further evaluate the surface roughness evolution of FSS 430 during tensile deformation, a mathematic calculation was made to quantitatively describe the surface roughness. For homogeneous specimens stretched along RD, the surface roughness can be expressed as:

$$\begin{aligned} R_{af} &= \frac{c_{1f} + c_{2f} + \cdots + c_{nf}}{n} \\ &= \frac{(c_{01} + c_{d1}) + (c_{02} + c_{d2}) + \cdots + (c_{0n} + c_{dn})}{n} \\ &= R_{a0} + R_{ad} \end{aligned} \tag{17}$$

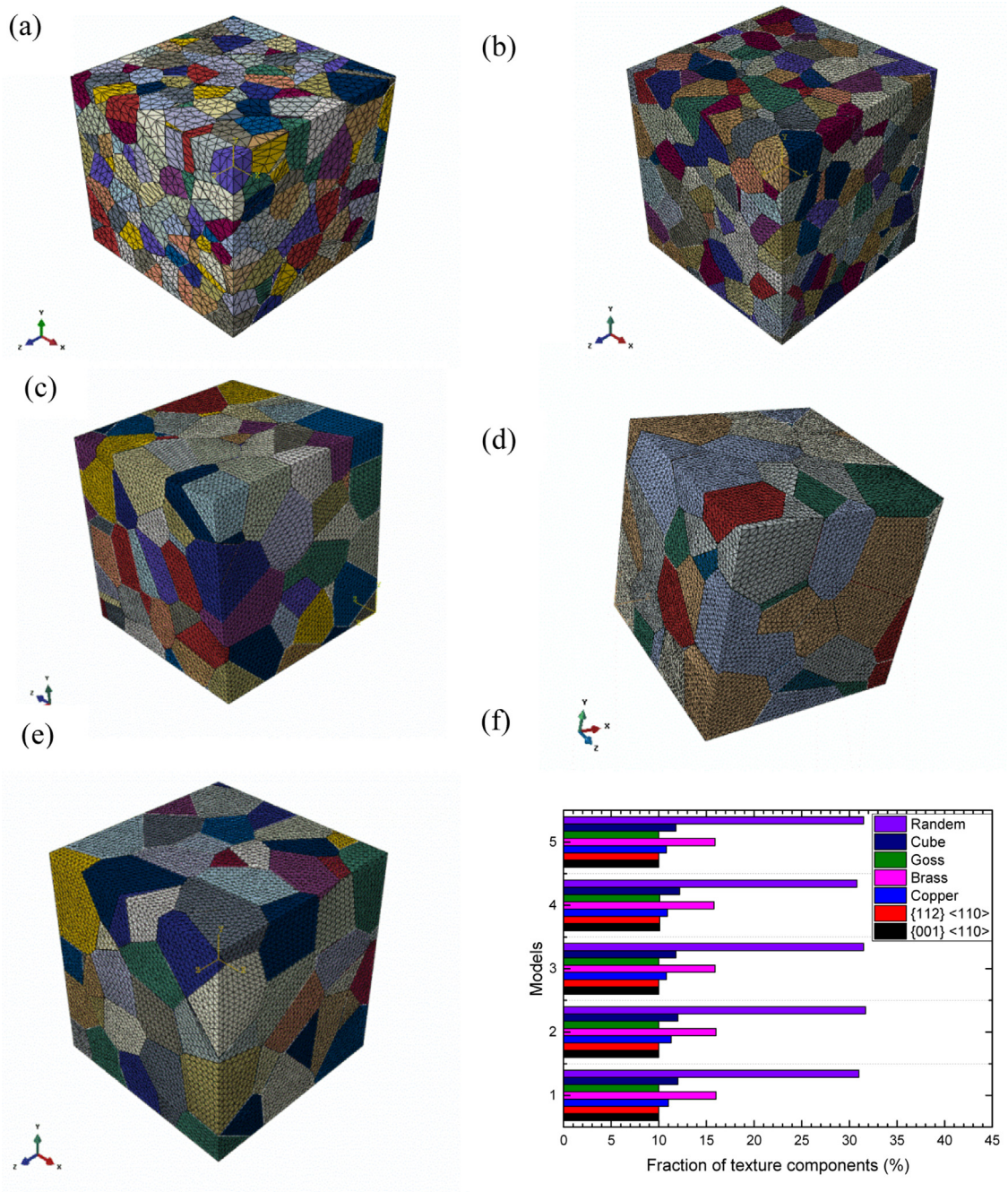

Fig. 7 – The surface topographies of established models with different average grain sizes: (a) 10 μm, (b) 12 μm, (c) 14 μm, (d) 16 μm and (e) 18 μm, and (f) the fraction of texture components in different models.

$$R_{qf} = \sqrt{\frac{c_{1f}^2 + c_{2f}^2 + \cdots + c_{nf}^2}{n}} = \sqrt{\frac{(c_{01} + c_{d1})^2 + (c_{02} + c_{d2})^2 + \cdots + (c_{0n} + c_{dn})^2}{n}} \sqrt{R_{q0}^2 + R_{qd}^2 + 2\frac{c_{01} * c_{d1} + c_{02} * c_{d2} + \cdots + c_{0n} * c_{dn}}{n}} \approx k_i * \sqrt{R_{q0}^2 + R_{qd}^2} \quad (18)$$

where k_i is a coefficient. The relationship between R_{qf}^2 and $(R_{q0}^2 + R_{qd}^2)$ is shown in Fig. 6. As can be seen from the curve, k_i equals to 1.0176 in the present work. Based on Eqs. (17) and (18), the final surface roughness (R_{af} and R_{qf} can be calculated by the initial surface roughness (R_{a0} and R_{q0}) and the difference of surface roughness (R_{ad} and R_{qd}). For homogeneous material sheet stretched along RD, the datum plane coefficients of the homogeneous deformation surface can be expressed as [27]:

$$R_{ad} = \frac{c_{d1} + c_{d2} + \cdots + c_{dn}}{n} = e^{-\mu\varepsilon_x} R_{a0} \quad (19)$$

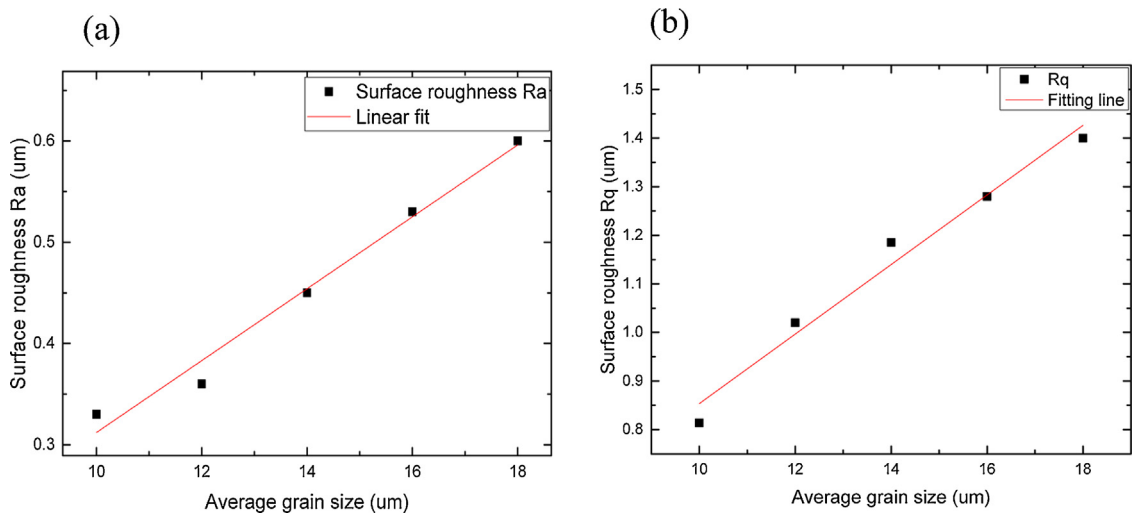

Fig. 8 – The relation between the average grain size and the surface roughness with the extension of 20%: (a) R_a and (b) R_q.

$$R_{qd} = \sqrt{\frac{c_{1d}^2 + c_{2d}^2 + \cdots + c_{nd}^2}{n}} = e^{-\mu\varepsilon_x} R_{q0} \tag{20}$$

where μ is the Poisson's ratio. Combining Eqs. (18) and (20), the final surface roughness can be calculated by the initial surface roughness. It can therefore be concluded that the initial surface roughness plays a significant role in determining the final surface roughness of FSS after forming process.

3.2. *Effects of grain size*

The surface deformation of polycrystalline materials can be described by the geometric non-uniform surface deformation and the anisotropic mechanical deformation. For FSS, crystals undergo rotation and movement during loading, causing the irregularity on the surface [18]. During the forming process, significant variations in the amount of localised deformation can be produced within the individual grains. The overlap and gap regions induced by the varying amounts of localised slip are accounted for through rearrangement of stored geometrically necessary dislocations [10]. Consequently, the neighbouring grains with different orientations exhibit different deformation during tension performance, causing corrugations on the surface of FSS sheets. The deformation of an individual grain is significantly dependent on grain size and orientation during loading. The grain sizes, therefore, play an important role in surface roughness evolution under the subsequent forming process.

A group of models with different average grain sizes are simulated to explore the effect of the average grain size on the surface roughness development of FSS. The results of EBSD tests indicate that the average grain size of cold-rolled FSS 430 ranges from 10 to 18 μm, the average grain sizes in models, therefore, are considered to be ranging from 10 to 18 μm. The initial surface roughness is proposed to be zero in all the models in this group. In addition, all the models are assigned the same fractions of texture components and five models are simulated in the present study (as shown in Fig. 7).

Table 3 – Values of surface roughness parameters obtained after regression analysis.

Parameters	k_{1s}	C_1	k_{2s}	C_2
Values	0.106	0.086	0.34	0.12

The relationship between the surface roughness and the average grain size with the extension of 20% is shown in Fig. 8. For the cold-rolled and annealed FSS 430 specimens, equixed grains are formed after recystallisation. The average grain size, therefore, can be utilised to describe the size of grains in FSS. As can be seen from the curve, a linear relationship between the surface roughness and the average grain size is obtained, which can be expressed as:

$$R_{qf0} = (k_{1s} \cdot D + C_1) * \varepsilon_x^2 \tag{21}$$

$$R_{qf0} = (k_{2s} \cdot D + C_2) * \varepsilon_x^2 \tag{22}$$

where D is the average grain size of FSS 430, and C is a constant. The slope of the curve is defined as k_s. The values of k_s and C are shown in Table 3. Based on Eqs. (21) and (22), the surface roughness after tensile deformation can be evaluated in combination with the average grain size of cold-rolled FSS 430. The grain refinement, therefore, is considered to be effective to reduce the surface roughness of FSS 430 during the forming process.

3.3. *Effects of textures*

During the forming process, the deformation of grains of FSS can be significantly affected by the crystallographic orientations [1–3]. To analyse the effects of textures on the surface roughness evolution, grains with six different texture components are simulated after tensile deformation (as shown in Fig. 9). The results indicate that the strain distributions and the deformation of grains are affected by textures. The strains are homogeneously distributed in models, this means that the surface roughness after plastic deformation is caused

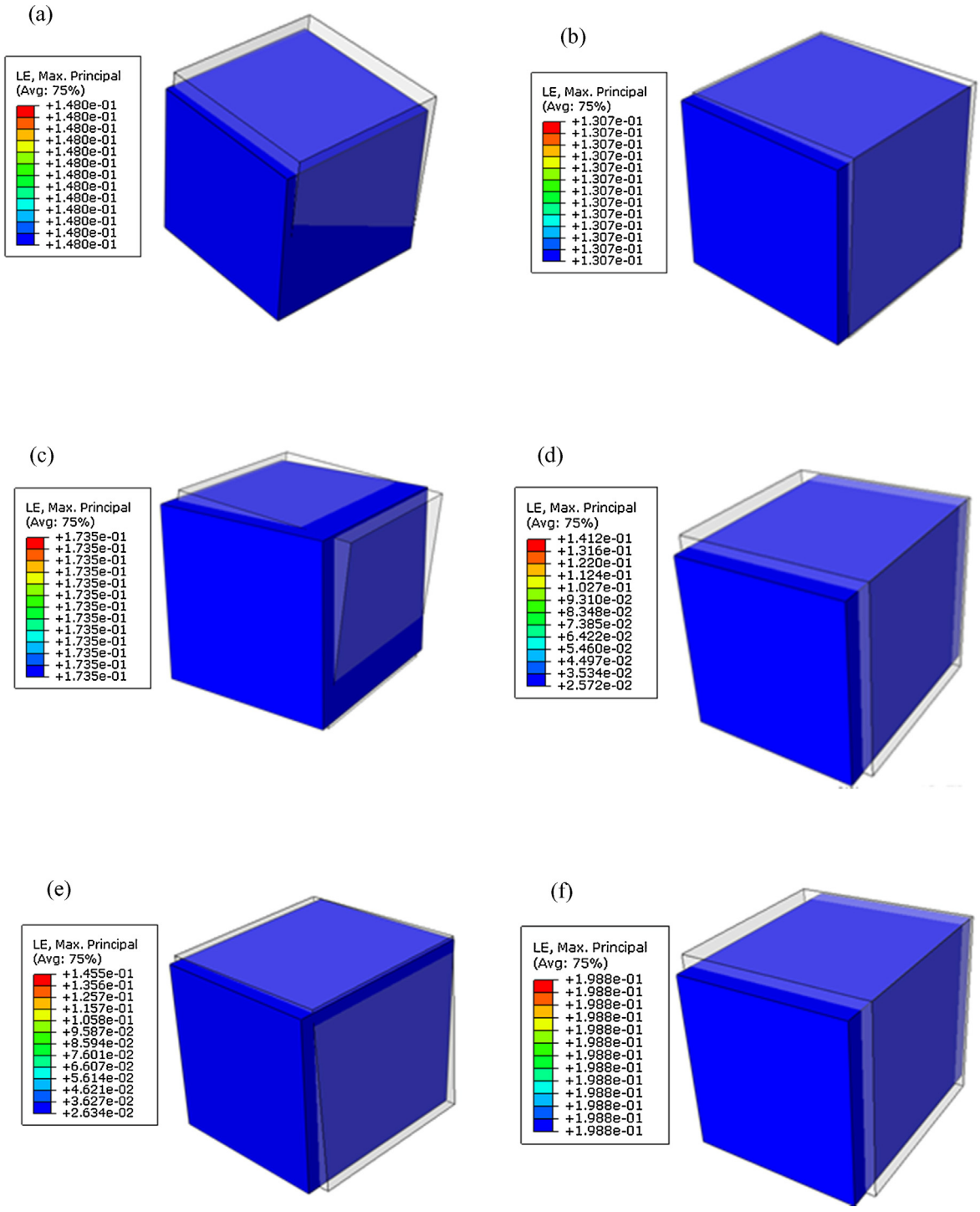

Fig. 9 – The deformed and undeformed shapes and strain distributions of models with different textures: (a) brass, (b) cube, (c) copper, (d) Goss, (e) {112}⟨110⟩, and (f) {001}⟨110⟩.

by the differential of crystal orientations between neighbouring grains. For grains with the same orientations, the strain localisation is eliminated on the free surface after tensile deformation. Thus, the homogeneity of crystallographic orientation is considered to have a significant influence on the surface roughness evolution of FSS after tensile deformation.

After tensile deformation, different texture components can induce various yielding based on Hall–Petch effect [13]. Thus, a further discussion is made to identify the effect of major textures on the surface roughness evolution. As shown in Fig. 9(a), significant shrink can be observed on the surface of grains with the {001}⟨110⟩ component. Compared with other typical BCC texture components, {001}⟨110⟩ orientation shows the minimum stored energy and lower plastic resistance [28]. As a consequence, the deformation of the {001}⟨110⟩ component can be critical, causing irregularity on the surface of FSS.

Table 4 – Calculated R-value of texture components.

Texture component	R-value (RD)	r-value (45°)	r-value (TD)
{001}⟨110⟩	0.00	1.00	0.00
{011}⟨100⟩	1.00	0.40	Infinite
{001}⟨100⟩	1.00	0.00	1.00
{112}⟨110⟩	0.11	6.00	1.00
Copper	1.00	5.99	0.11

Given that the deformation of grains with the {001}⟨110⟩ component is much larger than that of adjacent grains, remarkable corrugation is generated on the surface of FSS during the forming process. Unlike the {001}⟨110⟩ components, the effects of the Goss and the Cube components on surface roughness evolution are quite small (as shown in Fig. 9(e) and (f)). The Goss grains are mainly generated combining with the shear bands that developed in the late stages of the rolling processes [29], and the formation of shear bands may lead to shear deformation, preventing the formation of corrugation on the surface of FSS. In order to evaluate the plastic resistance of texture components, the plane strain ratio (*R*-value) of crystallographic orientations was calculated. Table 4 shows the *R*-value of major texture components. It can be seen that the *R*-value of the {001}⟨110⟩ and {112}⟨110⟩ components stretched along RD is lower than that of other major components, causing different plastic deformations of grains with different crystal orientations. It can therefore be concluded that the {001}⟨110⟩ and {112}⟨110⟩ components contribute to the surface roughening of FSS.

For evaluating the plastic resistance of texture components, the plane strain ratio of crystalline orientations was calculated. The results indicate that the strain ratio of major texture components stretched along RD is lower than that of other major components, inducing different plastic deformations of grains with different crystal orientations. The texture components, therefore, contribute to the surface roughening of FSS.

Table 5 – Surface roughness and average grain size of the specimens for tensile tests.

Sample	Cold-rolled FSS 430
Initial surface roughness (R_a/μm)	0.82
Initial surface roughness (R_q/μm)	1.07
Initial surface roughness (R_{sk}/μm)	−0.38
Initial surface roughness (R_{ku}/μm)	3.86
Average grain size (μm)	14.2

4. Surface roughness of FSS after tension performance

The uniaxial tensile tests were performed using INSTRON tensile testing machine and the samples were stretched along RD with the strain rate of $6.6 \times 10^{-4}\,s^{-1}$. The tensile tests follow ASTM-E8M Standard [30], and the dimensions of the tensile specimens are shown in Fig. 10. The initial surface roughness and the average grain size of the specimens were measured before tensile tests, and the results are listed in Table 5.

A comparison was made between the results from numerical simulation and practical tensile tests in order to verify the conclusions made in previous section. Combining Eqs.

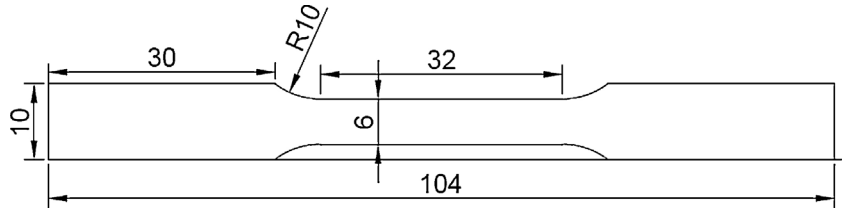

Fig. 10 – Dimensions of the specimen used for tensile tests.

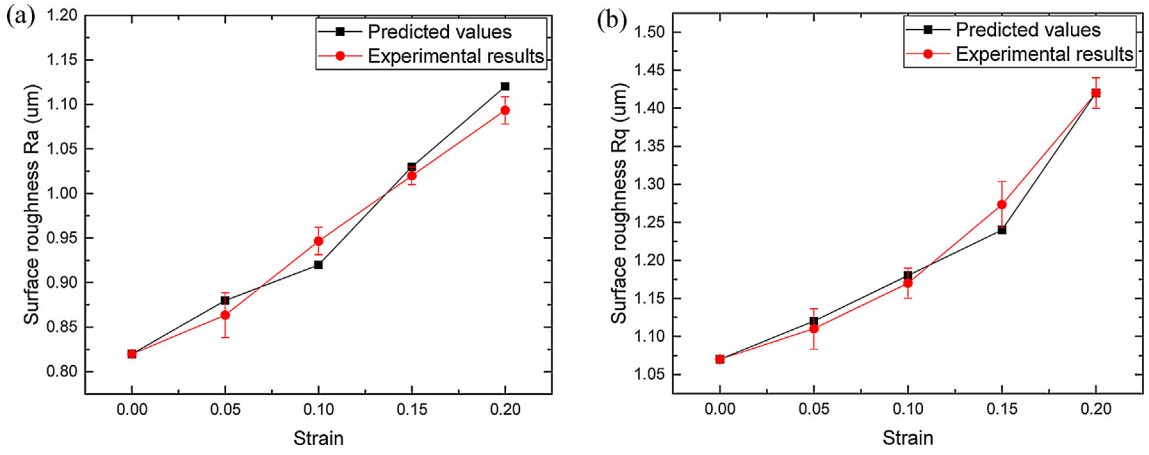

Fig. 11 – Comparison of surface roughness between numerical and experimental results (a) R_a and (b) R_q.

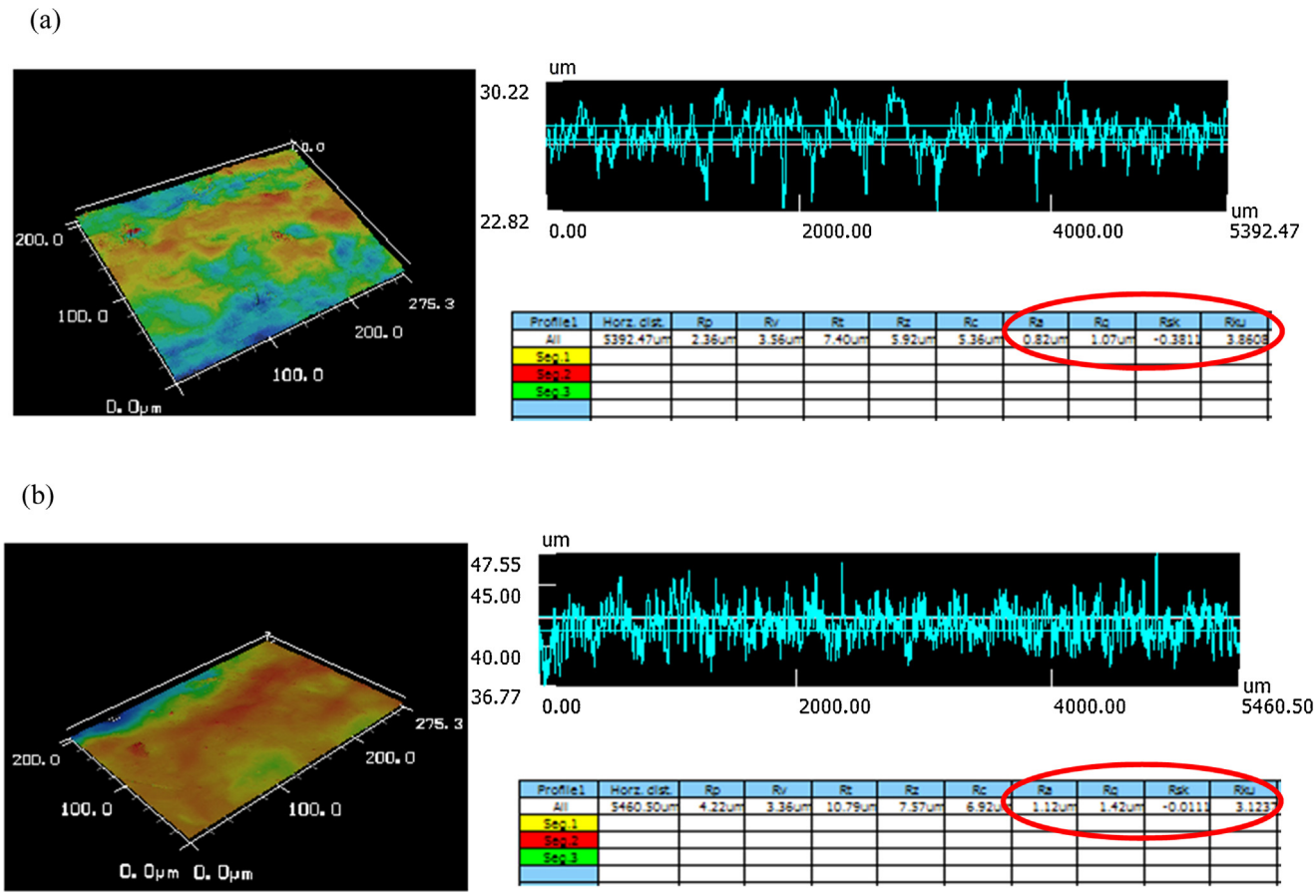

Fig. 12 – Evolution of surface topography of specimen: (a) without tensile deformation, and (b) after 20% extension.

(17)–(22), a quantitative description of the surface roughness after tensile test in RD is obtained, which can be expressed as:

$$R_{af} = (k_{1s} * D + C)\,\varepsilon_x^2 + e^{-\mu\varepsilon_x} * R_{q0} \tag{23}$$

$$R_{af} = \sqrt{\left[(k_{2s} * D + C)\,\varepsilon_x^2\right]^2 + \left[k_i\left(e^{-\mu\varepsilon_x} * R_{q0}\right)\right]^2} \tag{24}$$

Based on Eqs. (23) and (24), the surface roughness of FSS 430 after tensile tests can be evaluated. Fig. 11 compares the values of surface roughness that are obtained by numerical simulation and experimental tests. In addition, the evolution of surface topography is shown in Fig. 12. It can be seen from the curves that the simulated values of surface roughness match well with the experimental results. The proposed model and equations, therefore, can be utilised to evaluate the surface roughness of FSS 430 after uniaxial tensile tests.

5. Conclusions

In this work, CPFEM has been utilised to evaluate the surface roughness of FSS 430 after tensile deformation along RD. A quantitative equation was proposed to evaluate the surface roughness of FSS 430, and the effects of the initial surface roughness, average grain size and texture components on the surface roughening are numerically and experimentally investigated. Several conclusions can be drawn as follows:

(1) The final surface topography after tensile tests is mainly dependent on the homogeneous deformation and the inhomogeneous strain localisation. The corrugation on the surface of polycrystalline materials is significantly affected by the misorientations between neighbouring grains.
(2) A quantitative description of surface roughness evolution during tension performance is established. Based on the initial surface roughness, extension and the average grain size, the final surface roughness of FSS 430 after tensile deformation can be evaluated based on the proposed model. The experimental result matches well with the predicted values, indicating that the model can be utilised to evaluate the surface roughness after uniaxial tension.
(3) The relationship between the grain sizes, initial surface roughness, texture components and final surface roughness are analysed based on proposed model. A quadratic correlation between ΔR_a (ΔR_q) and tension strain is found to describe the surface roughness evolution of FSS 430 with ideal flat surface. In addition, the average grain size is found to be in the order of the surface roughness. The results also indicated that the refinement of texture benefits the final surface topography. The refinement of microstructure, therefore, is considered to be critical in

improving the surface quality of FSS 430 during the forming process.

Conflicts of interest

The authors declare no conflicts of interest.

Acknowledgements

The first author would like to thank the financial support by IPTA scholarship from University of Wollongong for his PhD study. The study is also supported by Baosteel-Australia Joint Research and Development Centre (BAJC).

REFERENCES

[1] Romanova VA, Balokhonov RR, Schmauder S. Numerical study of mesoscale surface roughening in aluminum polycrystals under tension. Mater Sci Eng A 2013;564:255–63.
[2] Takechi H, Kato H, Sunami T, Nakayama T. The mechanism of ridging phenomenon in 17% chromium stainless steel sheets. Trans JIM 1967;31:717–23.
[3] Wright RN. Anisotropic plastic flow in ferritic stainless steels and the roping phenomenon. Mater Sci Forum 1994;157:1137–44.
[4] Shin HJ, An JK, Park SH, Lee DN. The effect of texture on ridging of ferritic stainless steel. Acta Mater 2003;51:4693–706.
[5] Knutsen RD, Wittridge NJ. Modelling surface ridging in ferritic stainless steel. Mater Sci Technol 2002;18:1279–85.
[6] Jung I, Mola J, Chae D, De Cooman BC. Influence of the cold rolling and annealing sequence on the ridging behaviour of Ti-stabilised 18%Cr ferritic stainless steel. Steel Res Int 2010;81:1089–96.
[7] Shi Y, Jin H, Wu P, Lloyd D. Analysis of roping in an AA6111 T4P automotive sheet in 3D deformation states. Acta Mater 2017;124:598–607.
[8] Engler. Simulation of rolling and recrystallization textures in aluminium alloy sheets. Mater Sci Forum 2007;550:23–34.
[9] Huh M, Lee J, Park S, Engler O, Raabe D. Effect of through-thickness macro and micro-texture gradients on ridging of 17%Cr ferritic stainless steel sheet. Steel Res Int 2005;76:797–806.
[10] Stoudt M, Ricker R. The relationship between grain size and the surface roughening behaviour of Al–Mg alloys. Metal Mater Trans A 2002;33:2883–9.
[11] Stoudt M, Hubbard J, Iadicola M, Banovic S. A study of the fundamental relationships between deformation-induced surface rougheness and strain localisation in AA5754. Metal Mater Trans A 2009;40:1611–22.
[12] Wouters O, Vellinga W, Tijum R, Hosson J. On the evolution of surface roughness during deformation of polycrystalline aluminium alloys. Acta Mater 2005;53:4043–50.
[13] Ma X, Zhao J, Du W, Zhang X, Jiang L, Jiang Z. An analysis of ridging of ferritic stainless steel 430. Mater Sci Eng A 2017;685:358–66.
[14] Lefebvre G, Sinclair C, Lebensohn R, Mithieux J. Accounting for local interactions in the prediction of roping of ferritic stainless steel sheets. Model Simul Mater Sci Eng 2012;20:1–16.
[15] Saleh A, Pereloma E, Gazder A. Microstucture and texture evolution in a twinning induced-plasticity steel during uniaxial tension. Acta Mater 2013;61:2671–91.
[16] Qin L, Seefelde M, Houtte P. Analysis of roping of aluminium sheet materials based on the meso-scale moving window approach. Acta Mater 2015;84:215–28.
[17] Romanova V, Balokhonov R, Zinovieva O, Shakhijanov V. Numerical study of the surface-hardening effect on surface phenomena in 3D polycrystalline specimens. In: International conference on physical mesomechanics of multilevel systems. 2014.
[18] Pierce D, Asaro RJ, Needleman A. Acta Metall 1982;30:1087–109.
[19] Jung J, Yoon J, Park H, Kim H. Effect of coarse precipitates on surface roughening of an FCC polycrystalline material using crystal plasticity. Comput Mater Sci 2017;126:121–31.
[20] Wu P, Lloyd D, Huang Y. Correlation of ridging and texture in ferritic stainless steel sheet. Mater Sci Eng A 2006;427: 241–5.
[21] Wu P, Jin H, Shi Y, Lloyd D. Analaysis of ridging in ferritic stainless steel sheet. Mater Sci Eng A 2006;423:300–5.
[22] Viana C, Pinto A, Candido F, Matheus R. Analysis of ridging in three ferritic stainless steel sheets. Mater Sci Technol 2006;22:293–300.
[23] Mola J, Jung I, Park J, Chae D, Cooman B. Ridging control in transformable ferritic stainless steels. Metall Mater Trans A 2012;43:228–44.
[24] Zhang L, Xu W, Liu C, Ma X, Long J. Quantitative analysis of surface roughness evolution in FCC polycrystalline metal during uniaxial tension. Comput Mater Sci 2017;132: 19–29.
[25] Park S, Kim K, Lee Y, Park C. Evolution of microstructure and texture associated with ridging in ferritic stainless steels. ISIJ Int 2002;42:100–5.
[26] Patra S, Singhai L. Influence of hot band annealing and cold rolling on texture and ridging of 430 stainless steel containing aluminum. Mater Sci Appl 2013;4:70–6.
[27] Patra S, Ghosh A, Sood J, Singhai L, Podder A, Chakrabarti D. Effect of coarse grain band on the ridging severity of 409L ferritic stainless steel. Mater Des 2016;106:336–48.
[28] Mannan P, Saleh A, Gazder A, Casillas G, Pereloma E. Microstructure and micro-texture evolution during the dynamic recrystallization of a Ni–30Fe–Nb–C model alloy. J Alloys Compounds 2016;689:250–65.
[29] Dorner D, Zaefferer S, Raabe D. Retention of the Goss orientation between microbands during cold rolling of an Fe3%Si single crystal. Acta Mater 2007;55:2519–30.
[30] ASTM Standard E8-E8 M-08. Standard test methods for tension testing of metallic materials. West Conshohocken, PA: ASTM International; 2008.